

Triplet excitation and electroluminescence from a supramolecular monolayer embedded in a boron nitride tunnel barrier

Simon A. Svatek^{1*†}, James Kerfoot^{1†}, Alex Summerfield¹, Anton S. Nizovtsev^{2,3}, Vladimir V. Korolkov¹, Takashi Taniguchi⁴, Kenji Watanabe⁴, Elisa Antolín⁵, Elena Besley² and Peter H. Beton^{1*}

1. School of Physics and Astronomy, University of Nottingham, Nottingham, NG7 2RD, UK

2. School of Chemistry, University of Nottingham, Nottingham, NG7 2RD, UK

3. Nikolaev Institute of Inorganic Chemistry, Siberian Branch of the Russian Academy of Sciences, Academician Lavrentiev Avenue 3, 630090, Novosibirsk, Russian Federation

4. National Institute for Materials Science, 1-1 Namiki, Tsukuba, Ibaraki 305-0044, Japan.

5. Universidad Politécnica de Madrid - Instituto de Energía Solar, Avenida Complutense 30, 28040 Madrid, Spain

Abstract

We show that ordered monolayers of organic molecules stabilized by hydrogen bonding on the surface of exfoliated few-layer hexagonal boron nitride (hBN) flakes may be incorporated into van der Waals heterostructures with integral few-layer graphene contacts forming a molecular/2D hybrid tunneling diode. Electrons can tunnel from through the hBN/molecular barrier under an applied voltage V_{SD} and we observe molecular electroluminescence from an excited singlet state with an emitted photon energy $h\nu > eV_{SD}$, indicating up-conversion by energies up to ~ 1 eV. We show that tunnelling electrons excite embedded molecules into singlet states in a two-step process via an intermediate triplet state through inelastic scattering and also observe direct emission from the triplet state. These heterostructures provide a solid-state device in which spin-triplet states, which cannot be generated by optical transitions, can be controllably excited and provide a new route to investigate the physics, chemistry and

quantum spin-based applications of triplet generation, emission and molecular photon up-conversion.

Two-dimensional supramolecular arrays stabilised by non-covalent interactions provide a highly flexible route to the spatial organization, down to the molecular scale, of functional molecules on a surface^{1–4}. While this route to surface patterning has been successful in positioning chemical groups within adsorbed monolayers, the non-covalent nature of the stabilising interactions has limited the possibilities to explore the transport of charge through the component molecules. One possible route to explore the electrical properties of supramolecular monolayers is through the use of adjacent charge injection layers placed above and/or below the molecules. This architecture, in which current flows perpendicular to the plane of the adsorbed molecules, would require that the supramolecular layer is embedded in a more complex heterostructure with integral contact and spacer layers. Although there has been recent progress in the growth of all-organic epitaxial supramolecular heterojunctions^{5–7}, these structures cannot currently be prepared with the required complexity and control. The techniques used to fabricate van der Waals heterostructures⁸, such as a tunnel diode formed by placing few-layer hexagonal boron nitride (hBN) between two graphene layers⁹, offer an alternative approach. In this Letter we show that a similar device architecture may be employed to embed a supramolecular monolayer between two hBN tunnel barriers, thus forming a hybrid molecular/2D device. The encapsulated organic molecules can be excited electrically and subsequently relax through the emission of photons resulting in electroluminescence from both singlet and spin-triplet states. Photons are up-converted by energies up to 1 eV, and we show that singlets are excited through a multi-electron inelastic process via a triplet intermediate state. This hybrid structure provides a solid-state device in which triplets can be controllably excited, and offers a route to fundamental studies of long-lived excitations with non-zero spin and their relevance to low voltage light emitting devices, and quantum spin-based excitonic and electronic devices.

To fabricate our devices, we use polymer stamp-assisted van der Waals assembly^{10–12} to sequentially pick up flakes of few-layer graphene (FLG) and hBN. hBN flakes with adsorbed monolayers of organic molecules can be picked up and deposited as part of the assembly process in the same way as pristine flakes, thus allowing the integration of molecular layers within van der Waals heterostructures. We first use a polymer ‘stamp’ to pick up a large hBN

flake (lateral dimensions 10s of μm , thickness 10s of nm), which is ultimately used to cap the device. This hBN flake is then used to pick up a FLG flake which serves as the top contact, followed by a thin (≤ 1 nm) hBN flake which forms the upper tunnel barrier. The van der Waals stack is then used to pick up a second hBN tunnel barrier, also with a thickness of 1-3 monolayers, on which a molecular monolayer has been deposited by sublimation. This part-formed tunnelling device is then released from the stamp onto a second FLG flake which forms the lower contact; the release site is chosen so that the upper and lower FLG layers make independent contact with two pre-formed contacts (10 nm Cr/30 nm Au). Further details are provided in Supporting Information (SI).

A schematic of a completed device with an embedded monolayer of sublimed perylene tetracarboxylic di-imide (PTCDI) is shown in Figure 1a. The FLG provides semi-transparent top- and bottom-electrodes and the hBN layers allow carrier injection via tunnelling under an applied bias, while suppressing quenching from the FLG contacts¹³. PTCDI is a planar molecule and is adsorbed parallel to the hBN substrate in two-dimensional islands stabilised by hydrogen bonding¹⁴. The islands have monolayer height, typical lateral dimensions of 5 – 10 μm and, for the deposition parameters we use (see SI), a surface coverage of 50%. The molecular ordering within the islands is resolved using atomic force microscopy (AFM) which reveal lattice vectors close to the expected value¹⁴ (see Fig. 1b). At a large scale, individual monolayer PTCDI islands may be identified using optical microscopy during the transfer process (Fig. 1c). Images of a completed device are shown in Fig. 1d; the active area of the device (where the upper and lower FLG layers overlap) is marked. It is possible to selectively encapsulate a selected monolayer-height PTCDI island in the active region; for this device we used the island highlighted by an arrow in Fig. 1c which had been adsorbed on a bilayer hBN flake which forms the lower tunnel barrier. The effective area of the device is estimated to be 4 μm^2 . The deposition of PTCDI, and the preparation of the hBN surface is discussed in SI.

The current-voltage characteristics of the device were measured in an optical cryostat at a temperature $T = 6 \pm 1$ K, and are highly non-linear as expected for a tunnelling device (see Fig. 1f). The devices emit light when a current flows. The electroluminescence (EL) spectrum

acquired for an applied bias $V_{SD} = -3.3$ V (Fig. 1e) shows an intense peak at a wavelength 586.1 ± 0.5 nm (2.115 ± 0.002 eV) corresponding to the zero phonon transition (0-0) from the lowest excited singlet, S_1 , to the ground state, S_0 , accompanied by a satellite vibronic 0-1 peak (633.4 ± 0.5 nm/ 1.958 ± 0.002 eV). An optical image of the device under bias confirms that the active region of the device is the source of the photon emission (Fig. 1d). EL emission is observed in both polarities and the peak position varies by less than 0.5 nm over the measured voltage range (see Figure 2).

The EL peaks are close to the 0-0 transition (588.1 ± 0.5 nm/ 2.108 ± 0.002 eV) in the photoluminescence (PL) spectrum of the device (Fig. 1e). However both the PL and EL peaks are shifted from the 0-0 transition (565.0 ± 0.5 nm/ 2.194 ± 0.002 eV) measured for uncapped PTCDI (also shown in Fig. 1e) on a single hBN layer by 0.086 ± 0.003 eV (EL and PL spectra are also readily acquired at room temperature; the PL peak positions are independent of voltage – see SI). We have previously shown that, for uncapped PTCDI on hBN, a combination of resonant and non-resonant interactions between adsorbed PTCDI and hBN leads to a red-shift of 0.31 eV compared with gas phase spectra^{15,16}. A further red-shift is expected when a second hBN layer is added in the encapsulation process due to the additional changes in dielectric environment. This is discussed in more detail in SI where we calculate the transition energies of uncapped (2.26 eV) and capped (2.20 eV) PTCDI, and, in particular, a predicted red shift, 0.06 eV, due to the addition of a second hBN layer; these values are in good agreement with our experimental values.

The EL spectrum of PTCDI exhibits significant up-conversion, that is emission of photons with energies $h\nu > eV_{SD}$, the energy gained by an electron when passing between the two contacts¹⁷. This implies that the emission must occur through a multi-electron process, rather than through simple charge injection into the HOMO and LUMO levels of the molecule (as might be expected for a molecular analogue of a van der Waals heterostructure with a transition metal dichalcogenide emissive layer¹³), and is suggestive of an inelastic scattering mechanism. Figure 3a shows spectra acquired in this voltage range and we see a significant intensity in the 0-0

peak down to $|V_{SD}| = 1.6$ V, and at room temperature (see SI) down to 1.3 V implying an up-conversion energy close to 1 eV.

The observation of photon up-conversion indicates that molecules are excited into an intermediate state and then, through a further excitation, are excited into the singlet excited state S_1 . Electroluminescence is observed in this device for a current density down to ~ 1 pA nm^{-2} , which corresponds, approximately, to an average time between the traversal of electrons through each molecule of order 0.1 μs (assuming ~ 1 $\text{nm}^2/\text{molecule}$). The relevant excitation for the above-threshold emission must have a lifetime of this order of magnitude (or longer) thus ruling out mechanisms such as the sequential excitation of vibronic modes of the S_0 electronic ground state which relax on a much more rapid timescale. In common with Chen et al.¹⁸ we suggest that the long lifetime strongly suggests that the intermediate state involved in photon up-conversion is a T_1 spin-triplet.

The role of triplets is confirmed through the identification of an additional peak in the EL spectrum at $\sim 1004 \pm 1$ nm, photon energy 1.235 ± 0.001 eV. This peak is not present in the PL spectrum (see Fig. 3a inset), but is close to the value, 1.18 eV, of the triplet state of a related PTCDI derivative determined¹⁹ by triplet pair absorption. Accordingly we attribute this peak to emission from the T_1 state. The observed energy is also close to the energy, 1.29 eV, calculated for this transition (see SI).

Figure 3b shows that the emission intensities $I(T_1)$ and $I(S_1)$ from, respectively, the T_1 and S_1 states have a highly non-linear dependence on current. A logarithmic plot (Fig. 3c) shows a power law dependence of $I(S_1)$ on $I(T_1)$ over a large voltage range in both forward and reverse bias, $I(S_1) \propto I(T_1)^k$ where $k \approx 1.2$ indicating a near linear relationship. Assuming that, for a given applied voltage, the number of excited triplets is proportional to the T_1 intensity, triplet-triplet annihilation²⁰ may be ruled out as a route to the secondary excitation of molecules from T_1 to S_1 , since for this mechanism a quadratic dependence ($k \geq 2$) on the number of triplets would be expected. We therefore suggest that the T_1 to S_1 transition is promoted by a second inelastic electron scattering event.

The proposed mechanism is summarised in the band diagrams shown in Figures 4a and b. No emission is expected until the energy gained by tunnelling electrons, eV_{SD} exceeds the energy difference between the S_0 and T_1 states thus permitting excitation between these states through an inelastic process. We also see evidence for inelastic scattering in the electrical characteristics of the device. Figure 4c shows that a broad peak is observed in the second derivative of d^2I/dV^2 at ~ 1.1 V, very close to the triplet energy. Peaks in d^2I/dV^2 due to inelastic electron scattering are expected when the voltage drop matches the energy of an excitation to which electrons are coupled^{21,22} (similar features in hBN/graphene tunnel devices are observed to inelastic scattering of phonons²³). Molecules in the T_1 state may undergo a further inelastic excitation to the S_1 state or relax via the emission of a photon. This simple model is consistent with the voltage thresholds, peak energies and variation of intensity ratio which we observe and implies that the inelastic scattering process induces a change in the spin state of the molecule.

The generation of excitons in our devices shows fundamental differences to the mechanism in conventional organic light emitting diodes (OLEDs) where electrons and holes are injected from remote contacts and combine to form both singlet and triplet excitons. The spin degeneracy of these states typically leads²⁴ to a relative population of singlets and triplets in a ratio 1:3. The close proximity of the charge injection layers (~ 1 nm) to the emissive monolayer in our devices provides a different route which leads to the selective excitation of spin triplets.

While the architecture of our devices is significantly different to conventional OLEDs, we draw analogies with luminescence generated by the tip of a scanning tunnelling microscope^{25,26} (STML) for which the electrodes and photon source are also in close proximity and, moreover, the widely-accepted mechanism for molecular excitation in STML is via inelastic scattering and there are reports of photon up-conversion^{27–29}. The coupling of tip-induced localised plasmons to an adsorbed molecule is considered to be the most significant STML emission process²⁵; this is unlikely to be significant in our devices since the plasmon energy is much smaller³⁰ (in the range of 100s of meV) for our FLG contacts. However, recent papers have highlighted the role of triplets in STML. Specifically T_1 emission³¹ has been observed in the STML from perylene

tetracarboxylic dianhydride (PTCDA), although the proposed mechanism involves a charged molecule and is not accompanied by up-conversion. A triplet-mediated process has been proposed for the up-conversion in the STML of metal-free phthalocyanine¹⁸; this mechanism is similar to that discussed above but it is not accompanied by triplet emission.

These molecular/2D hybrid heterostructures provide an alternative electronic method to control the excitation of triplets, a transition which is optically forbidden, and offer a route to fundamental studies of long-lived optical excitations and their applications in quantum and spin based optoelectronics, and are also relevant to low voltage light emitting devices. The device architecture has many possible variations in the choice of contact materials, molecules with higher/lower energy levels, tunnel barrier width to control the current density, as well as the scaling of the active region down to a single or small ensemble of molecules. We also envisage the integration of molecular layers with more complex multilayer and/or in-plane supramolecular order to control the coupling of neighbouring molecular emitters. These solid state devices thus provide a new route to the investigation of the physics, chemistry and optoelectronic applications of triplet generation, emission and up-conversion.

ASSOCIATED CONTENT

Supporting Information

The Supporting Information is available free of charge on the ACS Publications website at DOI: *to be confirmed*.

Data Availability

The raw data for the AFM images and the optical and electrical measurements may be accessed through the University of Nottingham Research Data Management Repository at *doi to be registered*.

AUTHOR INFORMATION

Corresponding Authors

*e-mail: simon.svatek@upm.es and peter.beton@nottingham.ac.uk

Author Contributions

†These authors made equal contributions to this work.

ACKNOWLEDGMENTS

This work was supported by the Engineering and Physical Sciences Research Council [grant number EP/N033906/1]; and the Leverhulme Trust [grant number RPG-2016-104]. K.W. and T.T. acknowledge support from the Elemental Strategy Initiative conducted by the MEXT, Japan and the CREST (JPMJCR15F3), JST. E.A. is grateful for the Ramón y Cajal Fellowship funded by the Spanish MINECO. Computations were performed at the High Performance Computing facility at the University of Nottingham. We acknowledge the use of Athena at HPC Midlands+, which was funded by the EPSRC on grant EP/P020232/1 as part of the HPC Midlands+ consortium. We thank Bjarke Sørensen Jessen for helpful discussions.

REFERENCES

- (1) Mali, K. S.; Pearce, N.; De Feyter, S.; Champness, N. R. Frontiers of Supramolecular Chemistry at Solid Surfaces. *Chem. Soc. Rev.* **2017**, *46*, 2520–2542.
- (2) Macleod, J. M.; Rosei, F. Molecular Self-Assembly on Graphene. *Small* **2014**, *10*, 1038–1049.
- (3) Goronzy, D.; Ebrahimi, M.; Rosei, F.; Fang, Y.; Wee, A. T. S. A. T. S. A. T. S.; Feyter, S. De; Tait, S. L. S. L.; Wang, C.; Beton, P. H. P. H.; Weiss, P. S. P. S. P. S.; *et al.* Supramolecular Assemblies on Surfaces: Nanopatterning, Functionality, and Reactivity. *ACS Nano* **2018**, *12*, 7445–7481.
- (4) Auwärter, W.; Écija, D.; Klappenberger, F.; Barth, J. V. Porphyrins at Interfaces. *Nat. Chem.* **2015**, *7*, 105–120.
- (5) Korolkov, V. V.; Baldoni, M.; Watanabe, K.; Taniguchi, T.; Besley, E.; Beton, P. H. Supramolecular Heterostructures Formed by Sequential Epitaxial Deposition of Two-Dimensional Hydrogen-Bonded Arrays. *Nat. Chem.* **2017**, *9*, 1191–1197.
- (6) Schwarze, M.; Tress, W.; Beyer, B.; Gao, F.; Scholz, R.; Poelking, C.; Ortstein, K.; Gunther, A. A.; Kasemann, D.; Andrienko, D.; *et al.* Band Structure Engineering in Organic Semiconductors. *Science* **2016**, *352*, 1446–1449.
- (7) Chen, W.; Qi, D. C.; Huang, H.; Gao, X.; Wee, A. T. S. Organic–Organic Heterojunction Interfaces: Effect of Molecular Orientation. *Adv. Funct. Mater.* **2011**, *21*, 410–424.
- (8) Geim, A. K.; Grigorieva, I. V. Van Der Waals Heterostructures. *Nature* **2013**, *499*, 419–425.
- (9) Britnell, L.; Gorbachev, R. V.; Jalil, R.; Belle, B. D.; Schedin, F.; Mishchenko, A.; Georgiou, T.; Katsnelson, M. I.; Eaves, L.; Morozov, S. V.; *et al.* Field-Effect Tunneling Transistor Based on Vertical Graphene Heterostructures. *Science* **2012**, *335*, 947–950.
- (10) Pizzocchero, F.; Gammelgaard, L.; Jessen, B. S.; Caridad, J. M.; Wang, L.; Hone, J.; Bøggild, P.; Booth, T. J. The Hot Pick-up Technique for Batch Assembly of van Der Waals Heterostructures. *Nat. Commun.* **2016**, *7*.
- (11) Wang, L.; Meric, I.; Huang, P. Y.; Gao, Q.; Gao, Y.; Tran, H.; Taniguchi, T.; Watanabe, K.; Campos, L. M.; Muller, D. A.; *et al.* One-Dimensional Electrical Contact to a Two-Dimensional Material. *Science* **2013**, *342*, 614–617.
- (12) Kretinin, A. V.; Cao, Y.; Tu, J. S.; Yu, G. L.; Jalil, R.; Novoselov, K. S.; Haigh, S. J.; Gholinia, A.; Mishchenko, A.; Lozada, M.; *et al.* Electronic Properties of Graphene Encapsulated with Different Two-Dimensional Atomic Crystals. *Nano Lett.* **2014**, *14*, 3270–3276.
- (13) Withers, F.; Del Pozo-Zamudio, O.; Mishchenko, A.; Rooney, A. P.; Gholinia, A.; Watanabe, K.; Taniguchi, T.; Haigh, S. J.; Geim, A. K.; Tartakovskii, A. I.; *et al.* Light-

- Emitting Diodes by Band-Structure Engineering in van Der Waals Heterostructures. *Nat. Mater.* **2015**, *14*, 301–306.
- (14) Kerfoot, J.; Korolkov, V. V.; Svatek, S. A.; Alkhamisi, M.; Taniguchi, T.; Watanabe, K.; Parkinson, P. W.; Beton, P. H. Two-Dimensional Diffusion of Excitons in a Perylene Diimide Monolayer Quenched by a Fullerene Heterojunction. *J. Phys. Chem. C* **2019**, *123*, 12249–12254.
 - (15) Kerfoot, J.; Korolkov, V. V.; Nizovtsev, A. S.; Jones, R.; Taniguchi, T.; Watanabe, K.; Lesanovsky, I.; Olmos, B.; Besley, N. A.; Besley, E.; *et al.* Substrate-Induced Shifts and Screening in the Fluorescence Spectra of Supramolecular Adsorbed Organic Monolayers. *J. Chem. Phys.* **2018**, *149*, 054701.
 - (16) Wewer, M.; Stienkemeier, F. Laser-Induced Fluorescence Spectroscopy of N,N'-Dimethyl 3,4,9,10-Perylene Tetracarboxylic Diimide Monomers and Oligomers Attached to Helium Nanodroplets. *Phys. Chem. Chem. Phys.* **2005**, *7*, 1171–1175.
 - (17) Binder, J.; Howarth, J.; Withers, F.; Molas, M. R.; Taniguchi, T.; Watanabe, K.; Faugeras, C.; Wyszomolek, A.; Danovich, M.; Fal'ko, V. I.; *et al.* Upconverted Electroluminescence via Auger Scattering of Interlayer Excitons in van Der Waals Heterostructures. *Nat. Commun.* **2019**, 1–7.
 - (18) Chen, G.; Luo, Y.; Gao, H.; Jiang, J.; Yu, Y.; Zhang, L.; Zhang, Y.; Li, X.; Zhang, Z.; Dong, Z. Spin-Triplet-Mediated Up-Conversion and Crossover Behavior in Single-Molecule Electroluminescence. *Phys. Rev. Lett.* **2019**, *122*, 177401.
 - (19) Ford, W. E.; Kamat, P. V. Photochemistry of 3,4,9,10-Perylenetetracarboxylic Dianhydride Dyes. 3. Singlet and Triplet Excited-State Properties of the Bis(2,5-Di-Tert-Butylphenyl)imide Derivative. *J. Phys. Chem.* **1987**, *91*, 6373–6380.
 - (20) Uemura, T.; Furumoto, M.; Nakano, T.; Akai-Kasaya, M.; Saito, A.; Aono, M.; Kuwahara, Y. Local-Plasmon-Enhanced up-Conversion Fluorescence from Copper Phthalocyanine. *Chem. Phys. Lett.* **2007**, *448*, 232–236.
 - (21) Stipe, B. C.; Rezaei, M. A.; Ho, W. Single-Molecule Vibrational Spectroscopy and Microscopy. *Science* **1998**, *280*, 1732–1735.
 - (22) Adkins, C. J.; Phillips, W. A. Inelastic Electron Tunnelling Spectroscopy. *J. Phys. C Solid State Phys.* **1985**, *18*, 1313–1346.
 - (23) Vdovin, E. E.; Mishchenko, A.; Greenaway, M. T.; Zhu, M. J.; Ghazaryan, D.; Misra, A.; Cao, Y.; Morozov, S. V.; Makarovskiy, O.; Fromhold, T. M.; *et al.* Phonon-Assisted Resonant Tunneling of Electrons in Graphene–Boron Nitride Transistors. *Phys. Rev. Lett.* **2016**, *116*, 186603.
 - (24) Mitschke, U.; Bäuerle, P. The Electroluminescence of Organic Materials. *J. Mater. Chem.* **2000**, *10*, 1471–1507.

- (25) Kuhnke, K.; Große, C.; Merino, P.; Kern, K. Atomic-Scale Imaging and Spectroscopy of Electroluminescence at Molecular Interfaces. *Chem. Rev.* **2017**, *117*, 5174–5222.
- (26) Doppagne, B.; Chong, M. C.; Bulou, H.; Boeglin, A.; Scheurer, F.; Schull, G. Electrofluorochromism at the Single-Molecule Level. *Science* **2018**, *361*, 251–255.
- (27) Dong, Z. C.; Zhang, X. L.; Gao, H. Y.; Luo, Y.; Zhang, C.; Chen, L. G.; Zhang, R.; Tao, X.; Zhang, Y.; Yang, J. L.; *et al.* Generation of Molecular Hot Electroluminescence by Resonant Nanocavity Plasmons. *Nat. Photonics* **2010**, *4*, 50–54.
- (28) Peters, P.-J.; Xu, F.; Kaasbjerg, K.; Rastelli, G.; Belzig, W.; Berndt, R. Quantum Coherent Multielectron Processes in an Atomic Scale Contact. *Phys. Rev. Lett.* **2017**, *119*, 066803.
- (29) Xu, F.; Holmqvist, C.; Belzig, W. Overbias Light Emission Due to Higher-Order Quantum Noise in a Tunnel Junction. *Phys. Rev. Lett.* **2014**, *113*, 066801.
- (30) Low, T.; Avouris, P. Graphene Plasmonics for Terahertz to Mid-Infrared Applications. *ACS Nano* **2014**, *8*, 1086–1101.
- (31) Kimura, K.; Miwa, K.; Imada, H.; Imai-Imada, M.; Kawahara, S.; Takeya, J.; Kawai, M.; Galperin, M.; Kim, Y. Selective Triplet Exciton Formation in a Single Molecule. *Nature* **2019**, *570*, 210–213.

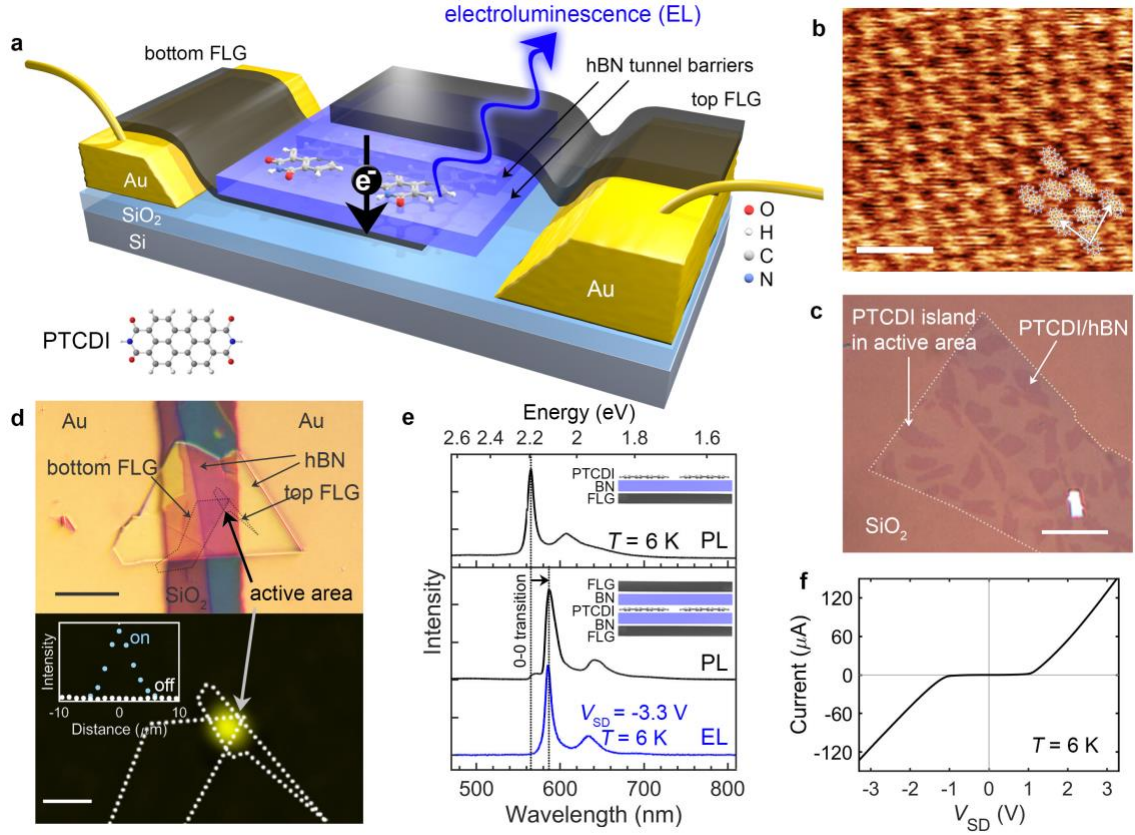


Figure 1. FLG/BN/PTCDI/hBN/FLG heterostructures. **a**, Schematic of a device in which a monolayer of PTCDI is encapsulated between two hBN tunnel barriers and charge is injected from upper and lower FLG contacts (the upper thick hBN layer, and a supporting thick hBN flake which provides a supporting substrate for the lower graphene are omitted for clarity; neither plays an active role in the device operation); lower left - schematic of the molecular structure of PTCDI. **b**, AFM image of a monolayer-thick island of PTCDI on hBN; the lattice vectors of the molecular array are marked and have the following values: 1.48 ± 0.1 nm and 1.78 ± 0.1 nm, subtended by an angle of 89° . **c**, Optical micrograph showing monolayer islands following sublimation of 0.5 monolayers of PTCDI on a bilayer hBN flake (highlighted by dotted outline); this flake forms the lower tunnel barrier for this device and the island selected for the active region is marked by an arrow – note that the PTCDI grows in a different morphology on the surrounding SiO₂ surface and cannot be resolved in these regions. **d**, upper - Optical image of a device showing gold contacts and van der Waals heterostructure. The active area of the device where the upper and lower FLG layers overlap is highlighted; lower - optical image of the device taken under bias ($V_{SD} = -3.2$ V) acquired with an exposure time of 8 s with an overlay also showing the position of the graphene contacts and confirming that light is emitted from the active area of the device; inset the variation of intensity along the horizontal axis through (on) and away (off) the active region. **e**, Electroluminescence (acquisition time 100 s) and photoluminescence spectra of device acquired at liquid helium temperatures; the PL for an uncapped device is also included highlighting the peak shift due to encapsulation. **f**, Current-voltage characteristics. Scale bars (b) 3 nm, (c) 20 μm, (d) 20 μm (upper) and 6 μm (lower).

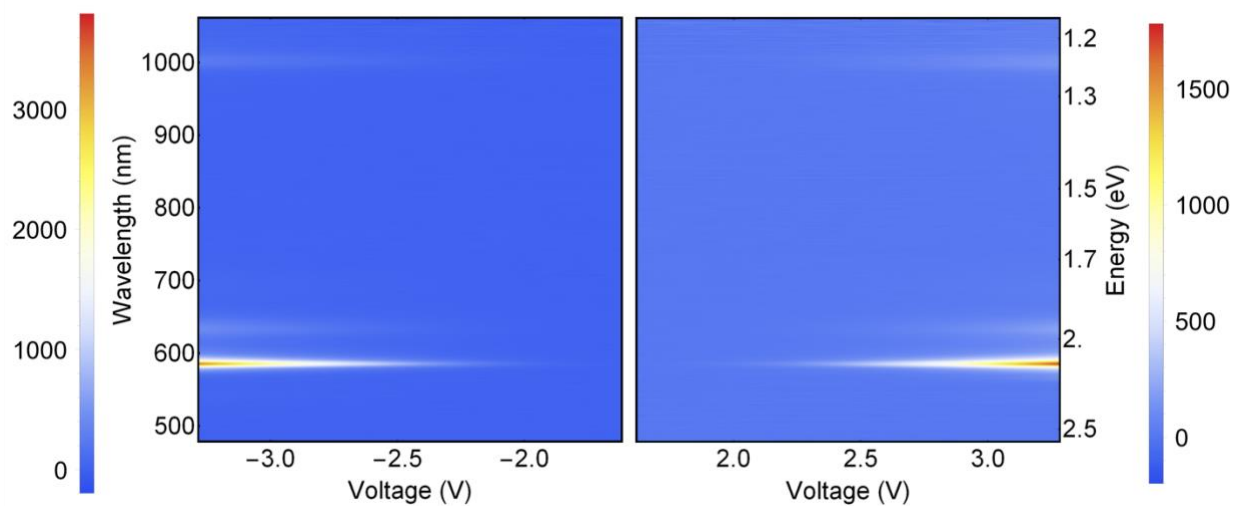


Figure 2. Voltage map of electroluminescence. The EL intensity is displayed as a colour map for different voltages (horizontal axis) and wavelengths (vertical axis). This data shows that the EL peak position is constant over the measured voltage range.

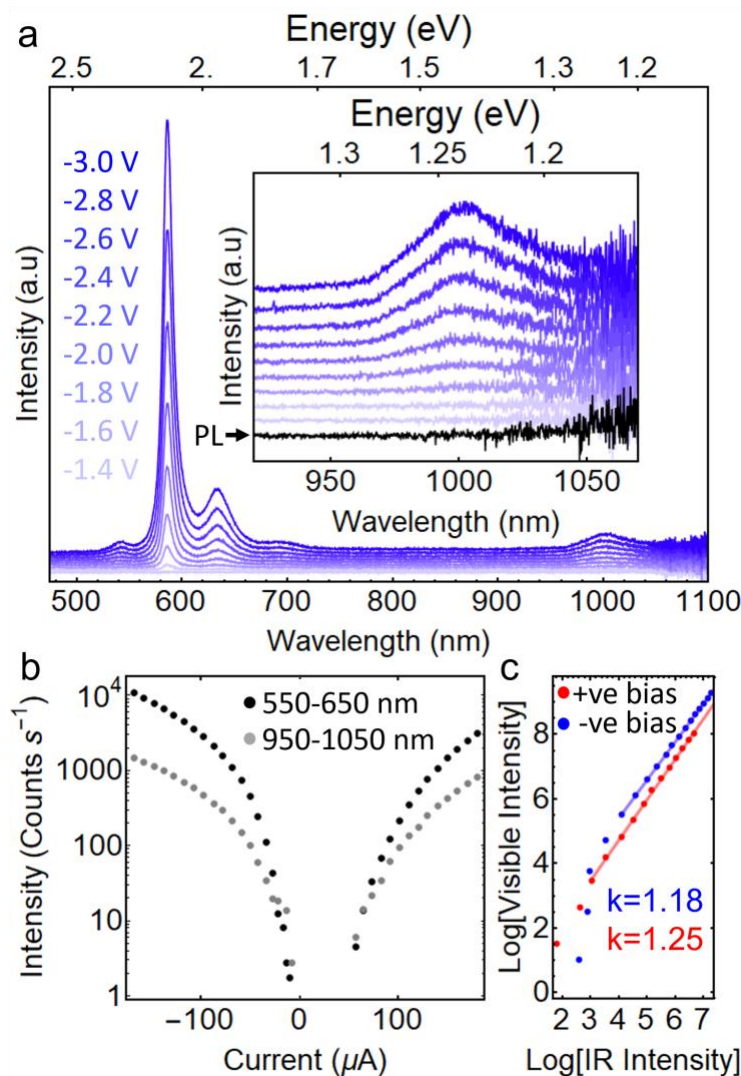


Figure 3. Photon up-conversion and triplet electroluminescence from a FLG/BN/PTCDI/hBN/FLG heterostructure. **a**, Spectra acquired at 6 K with a 100 second integration time for a series of applied voltages ranging from -1.4V to -3.0 V; inset - electroluminescence in the infra-red plotted together with the photoluminescence spectrum in the same spectral region (black). **b**, The electroluminescence signal (with background subtracted) integrated between 550 and 650 nm and 950 and 1050 nm, versus current. **c**, Logarithmic plot of the integrated intensity between 550 and 650 nm versus the intensity between 950 and 1050 nm showing a near-linear dependence between the singlet and triplet emission intensities.

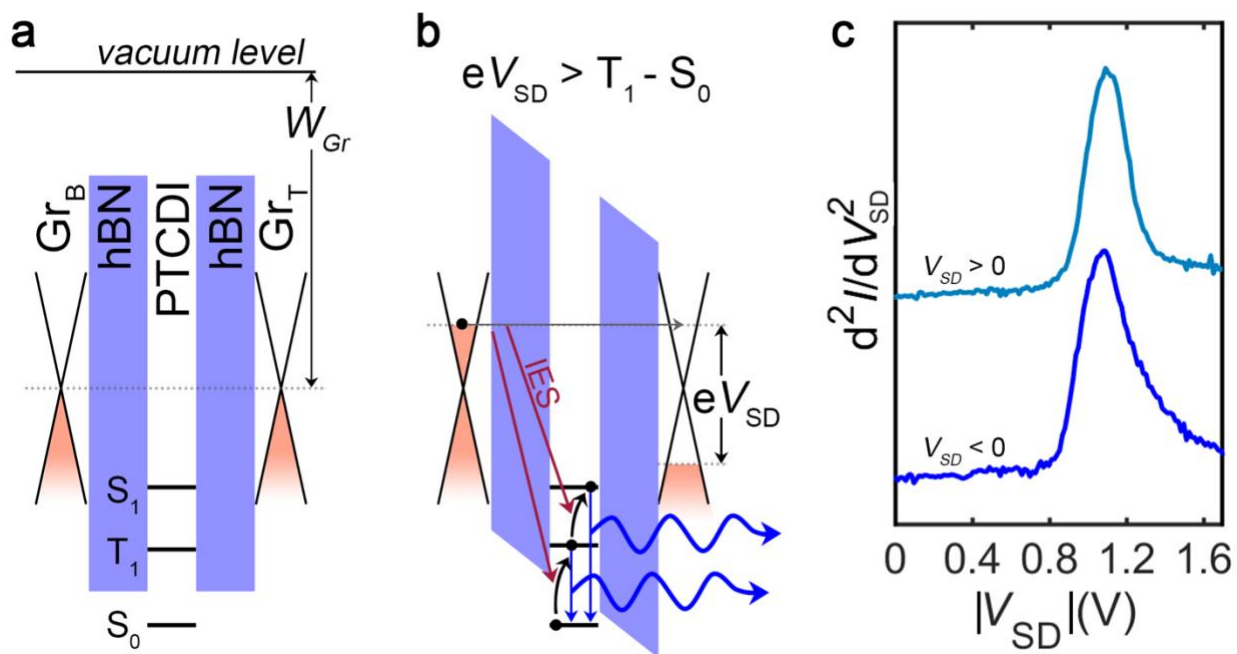


Figure 4. Mechanism and inelastic tunnelling spectroscopy. **a**, Alignment of work function of graphene (W_{Gr}), hBN bands and molecular energy levels under zero bias. **b**, Band alignment under bias V_{SD} ; molecule can be inelastically excited when eV_{SD} exceeds the energy difference between the S_0 and T_1 states. Molecule undergoes a further inelastic excitation to the S_1 state; photons can be emitted from a transition to S_0 from either the S_1 or T_1 states. **c**, Peaks in d^2I/dV^2 occur where eV_{SD} matches the energy of the excitation. Clear peaks are observed for $V_{SD} \approx 1.1$ V close to the value expected for triplet excitation via inelastic scattering.

Triplet excitation and electroluminescence from a supramolecular monolayer embedded in a boron nitride tunnel barrier

Simon A. Svatek^{1*†}, James Kerfoot^{1†}, Alex Summerfield¹, Anton S. Nizovtsev^{2,3}, Vladimir V. Korolkov¹, Takashi Taniguchi⁴, Kenji Watanabe⁴, Elisa Antolín⁵, Elena Besley² and Peter H. Beton^{1*}

Supporting Information

1. School of Physics and Astronomy, University of Nottingham, Nottingham, NG7 2RD, UK

2. School of Chemistry, University of Nottingham, Nottingham, NG7 2RD, UK

3. Nikolaev Institute of Inorganic Chemistry, Siberian Branch of the Russian Academy of Sciences, Academician Lavrentiev Avenue 3, 630090, Novosibirsk, Russian Federation

4. The National Institute for Materials Science, Advanced Materials Laboratory, 1-1 Namiki, Tsukuba, Ibaraki 305-0044, Japan

5. Universidad Politécnica de Madrid - Instituto de Energía Solar, Avenida Complutense 30, 28040 Madrid, Spain

*e-mail: simon.svatek@upm.es and peter.beton@nottingham.ac.uk

1. Calculation of shifts of PTCDI emission energy

The non-resonant shifts of the PTCDI fluorescence are calculated using time-dependent density functional theory (TD-DFT). Resonant shifts, which arise from the coupling of the transition dipole moment to both the dielectric environment and other molecules, are derived from the transition density and transition dipole moments calculated at the DFT level of theory.

1.1 Non-resonant shifts and triplet energy: density functional theory

The hBN surface was modelled by a flake consisting of 75 boron atoms and 75 nitrogen atoms with the edges capped by hydrogens. Atomic positions in the hBN flake were optimized at the ω B97X-D3-gCP/def2-SVP level of theory¹⁻⁶ and kept fixed in the subsequent calculations. The second hBN layer was placed parallel to the bottom hBN layer on top of the most energetically preferred adsorption site of PTCDI/hBN system determined for the S_0 , T_1 , and S_1 electronic states. The atomic positions of hBN and PTCDI/hBN fragments were fixed upon changing the distance between them.

The structural relaxation of the chemical systems under study in the S_1 state and excitation energies corresponding to absorption ($S_1 \leftarrow S_0$ transition), fluorescence ($S_0 \leftarrow S_1$ transition), and phosphorescence ($S_0 \leftarrow T_1$ transition) were calculated with TD-DFT using the TD- ω B97X-D3-gCP/def2-SVP protocol. The structure of compounds in the T_1 state was optimized at the ω B97X-D3-gCP/def2-SVP level of theory within the unrestricted Kohn-Sham formalism. The RI-JONX resolution of identity approximation was used to accelerate convergence, whereas the integration grid was controlled by grid6 keyword. Geometrical counterpoise correction (gCP) was applied throughout in order to remove artificial overbinding effects from the basis set superposition error⁶. Atomic partial charges were calculated within ChelpG formalism⁷. All calculations were performed with the ORCA 4.0 and ORCA 4.1 software packages⁸. Cube files with transition densities were generated using orca_plot utility with a step size of 0.1 Å in each direction.

The equilibrium structures of PTCDI molecule adsorbed on the hBN surface are shown in Figure S1. In the case of the S_1 structure, the mean molecule-surface separation is smaller by 0.13 Å in

comparison to the S_0 and T_1 structures. The energies of adsorption of PTCDI on the hBN in the S_0 , T_1 , and S_1 electronic states were computed to be 1.88 eV, 1.89 eV, and 1.93 eV, respectively.

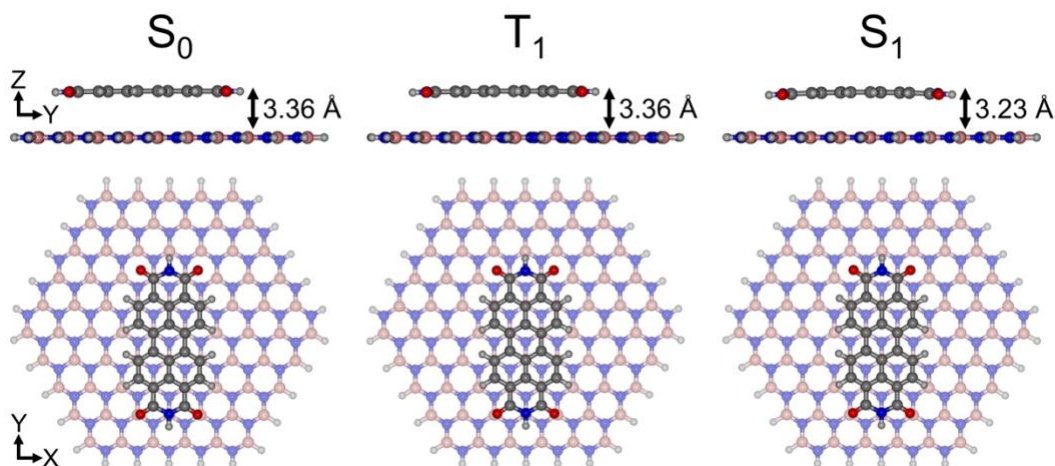
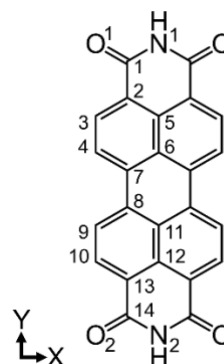


Figure S1. Relaxed structures of PTCDI/hBN in the S_0 , T_1 , and S_1 electronic states calculated at the (TD-) ω B97X-D3-gCP/def2-SVP level of theory. Mean molecule–surface distances are shown.

From Table S1 one can see that selected bond lengths of PTCDI change within 0.06 Å after an electronic excitation and the shortening of a single C–C bond in the center of molecule is the most notable variation. It should be mentioned that interaction with the surface has only minor effect on the bond distances in PTCDI and leads to slightly non-planar structure, reducing D_{2h} point group symmetry of the molecule to C_s .

Table S1. Selected bond lengths (r , Å) of PTCDI in the gas phase and adsorbed on hBN surface (in parentheses) in the S_0 , T_1 , and S_1 electronic states calculated at the (TD-) ω B97X-D3-gCP/def2-SVP level of theory.

| Bond X–Y | $r_{X-Y}(S_0)$, Å | $r_{X-Y}(T_1)$, Å | $r_{X-Y}(S_1)$, Å |
|----------------------------------|--------------------|--------------------|--------------------|
| N ₁ –C ₁ | 1.393 (1.393) | 1.392 (1.392) | 1.387 (1.386) |
| O ₁ –C ₁ | 1.210 (1.212) | 1.213 (1.215) | 1.212 (1.214) |
| C ₁ –C ₂ | 1.495 (1.494) | 1.487 (1.486) | 1.482 (1.480) |
| C ₂ –C ₃ | 1.380 (1.380) | 1.414 (1.414) | 1.399 (1.400) |
| C ₃ –C ₄ | 1.407 (1.407) | 1.371 (1.372) | 1.380 (1.380) |
| C ₂ –C ₅ | 1.424 (1.424) | 1.416 (1.416) | 1.413 (1.413) |
| C ₅ –C ₆ | 1.426 (1.426) | 1.442 (1.442) | 1.431 (1.431) |
| C ₄ –C ₇ | 1.390 (1.390) | 1.446 (1.446) | 1.424 (1.424) |
| C ₆ –C ₇ | 1.435 (1.435) | 1.426 (1.426) | 1.424 (1.424) |
| C ₇ –C ₈ | 1.484 (1.484) | 1.425 (1.425) | 1.441 (1.441) |
| C ₈ –C ₉ | 1.390 (1.390) | 1.446 (1.445) | 1.424 (1.424) |
| C ₉ –C ₁₀ | 1.407 (1.407) | 1.371 (1.372) | 1.380 (1.380) |
| C ₈ –C ₁₁ | 1.435 (1.435) | 1.426 (1.426) | 1.424 (1.424) |
| C ₁₁ –C ₁₂ | 1.426 (1.426) | 1.442 (1.442) | 1.431 (1.431) |
| C ₁₀ –C ₁₃ | 1.380 (1.380) | 1.414 (1.414) | 1.399 (1.400) |
| C ₁₂ –C ₁₃ | 1.424 (1.424) | 1.416 (1.416) | 1.413 (1.413) |
| C ₁₃ –C ₁₄ | 1.495 (1.494) | 1.487 (1.486) | 1.482 (1.480) |
| O ₂ –C ₁₄ | 1.210 (1.212) | 1.213 (1.215) | 1.212 (1.214) |
| N ₂ –C ₁₄ | 1.393 (1.393) | 1.392 (1.392) | 1.387 (1.386) |



The most intense band in the fluorescence spectra of isolated and adsorbed PTCDI arises from the electronic transition between the highest occupied (HOMO) and the lowest unoccupied (LUMO) molecular orbitals which have π and π^* character, respectively (Figure S2). The corresponding transition density of this dipole-allowed $S_0 \leftarrow S_1$ transition is presented in Figure S2. The first triplet excited state is also characterized by the HOMO–LUMO transition. Although the $S_0 \leftarrow T_1$ transition is spin-forbidden it has a low intensity and contributes to the experimental emission spectrum. To estimate the effect of spin-orbit coupling, which makes a singlet-triplet transition allowed, on the transition energy and transition dipole moment (μ) of the $S_0 \leftarrow T_1$ transition of PTCDI, quasi-degenerate perturbation theory was used in conjunction with TD-DFT.⁹ This effect turned out to be small ($\Delta E < 0.001$ eV, $\Delta\mu < 10^{-4}$ D) for the isolated molecule and therefore was not taken into account for other systems under study.

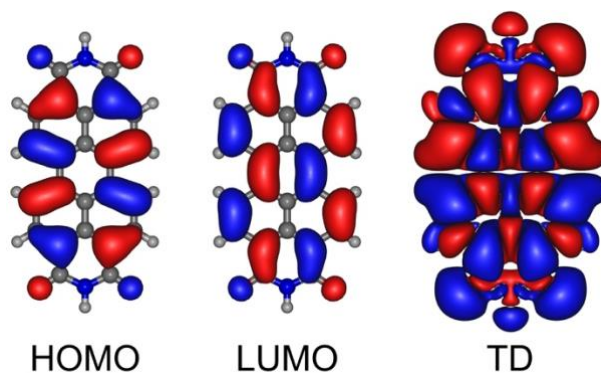


Figure S2. Highest occupied molecular orbital (HOMO), lowest unoccupied molecular orbital (LUMO), and transition density (TD) for the $S_0 \leftarrow S_1$ fluorescence process of PTCDI calculated at the (TD-) ω B97X-D3-gCP/def2-SVP level of theory. Isosurfaces with ± 0.02 a.u. and ± 0.0001 a.u. isovalues are shown for molecular orbitals and transition density, respectively.

Moving onto the hBN/PTCDI/hBN sandwich structures, we have computed potential energy curves (PECs) shown in Figure S3 in order to predict the equilibrium hBN–hBN distances. These were followed by the calculations of absorption ($S_1 \leftarrow S_0$), fluorescence ($S_0 \leftarrow S_1$), and phosphorescence ($S_0 \leftarrow T_1$) energies with the corresponding transition dipole moments and oscillator strengths for (i) free PTCDI molecule; (ii) PTCDI in the geometry optimized on hBN, but with the surface removed; (iii) PTCDI on the hBN surface; (iv) PTCDI between two hBN layers. The computed characteristics of these electronic transitions are summarized in Table S2; these are shown to agree well with the previously reported values.¹⁰

For PTCDI adsorbed on the hBN surface, the calculated position of maximum in the fluorescence spectrum is red-shifted by 0.12 eV as compared to PTCDI in gas phase. The addition of a second hBN layer on top of PTCDI is predicted to further increase the fluorescence red shift by 0.085 eV. To explain the origin of this additional contribution to the observed red shift in the fluorescence spectrum, which corresponds to a non-resonant shift, an energy decomposition of the shift into the contributions from molecular distortion (ΔE_{dist}), electrostatic (ΔE_{elec}) and chemical (ΔE_{chem}) interactions has been performed using Hochheim and Bredow approach¹¹ (see Table S3). It has been found that the orbital interactions between the PTCDI molecule and the atoms residing in the top hBN layer are responsible for the additional red shift reflected in the decrease in the value

of the fluorescence energy by 0.085 eV as compared to the PTCDI/hBN structure. Table S2 also shows that for a PTCDI molecule sandwiched between two hBN layers the calculated transition energy for the $S_0 \leftarrow T_1$ process is 1.29 eV as noted in the main text. In both phases the PTCDI is stabilized by hydrogen bonding which we have previously shown¹⁰ leads to a small additional red shift of the fluorescence by 0.03 eV, giving a total non-resonant shift of 0.150 eV and 0.235 eV respectively for adsorbed/encapsulated PTCDI.

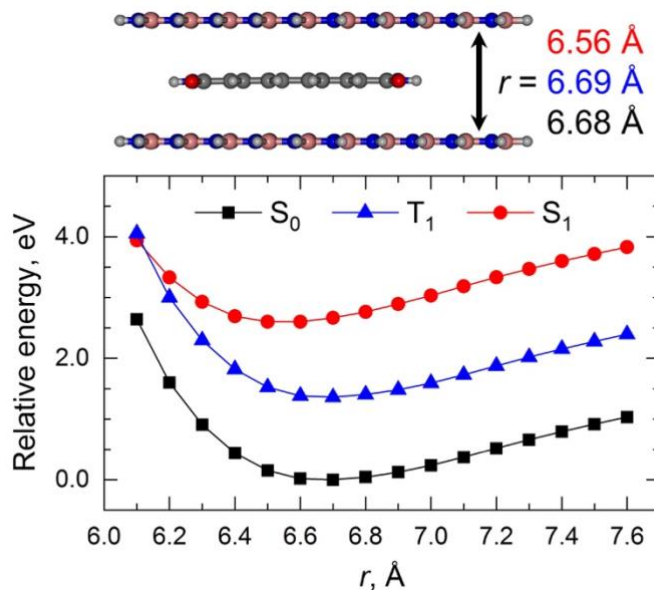


Figure S3. Calculated potential energy curves of the *hBN*/PTCDI/*hBN* sandwich structure in the S_0 , T_1 , and S_1 electronic states and the corresponding equilibrium interlayer distances (r , see color code). Relative energies are given with respect to the minimum of S_0 curve.

Table S2. Details of absorption ($S_1 \leftarrow S_0$), fluorescence ($S_0 \leftarrow S_1$), and phosphorescence ($S_0 \leftarrow T_1$) processes for free PTCDI molecule, PTCDI in the geometry optimized on hBN but with the surface removed (in round brackets), PTCDI on the hBN surface (in square brackets)^a and PTCDI between two hBN layers (in curly brackets)^b calculated at the (TD-) ω B97X-D3-gCP/def2-SVP//((TD-) ω B97X-D3-gCP/def2-SVP level of theory.

| | Absorption | Fluorescence | Phosphorescence |
|---|--|--|--|
| Transition energy, eV / nm | 2.975 / 417 (2.970 / 418) [2.869 / 432] {2.780 / 446} | 2.526 / 491 (2.517 / 493) [2.406 / 515] {2.321 / 534} | 1.272 / 975 (1.276 / 972) [1.283 / 966] {1.288 / 962} |
| Transition dipole moment, D | (0.00, 8.26, 0.00) ((0.00, 8.28, 0.03)) [(0.00, 7.26, 0.05)] {(0.00, 6.49, 0.06)} | (0.00, 8.83, 0.00) ((0.00, 8.85, 0.02)) [(0.00, 7.83, 0.05)] {(0.00, 7.08, 0.04)} | (0.00, 0.00, 0.00) ((0.00, 0.00, 0.00)) [(0.00, 0.00, 0.00)] {(0.00, 0.00, 0.00)} |
| Oscillator strength, au | 0.77 (0.77) [0.57] {0.44} | 0.75 (0.75) [0.56] {0.44} | 0.00 (0.00) [0.00] {0.00} |
| $E_{\text{HOMO}} / E_{\text{LUMO}}$, eV^c | -8.18 / -2.09 (-8.19 / -2.10) [8.07 / -2.04] {-7.97 / -2.01} | -7.93 / -2.45 (-7.93 / -2.46) [-7.82 / -2.41] {-7.72 / -2.36} | -7.79 / -2.62 (-7.80 / -2.63) [-7.69 / -2.56] {-7.60 / -2.51} |
| $\Delta E_{\text{HOMO-LUMO}}$, eV^c | 6.09 (6.08) [6.02] {5.96} | 5.48 (5.47) [5.41] {5.36} | 5.17 (5.17) [5.13] {5.09} |

^a Calculated mean PTCDI–hBN distances are 3.356 Å, 3.225 Å, and 3.360 Å for the S_0 , S_1 , and T_1 structures, respectively.

^b Transition energies were computed at the minima of the corresponding potential energy curves ($r(S_0) = 6.684$ Å, $r(S_1) = 6.558$ Å, $r(T_1) = 6.687$ Å).

^c Energies of the frontier molecular orbitals were calculated for the systems in the S_0 states using the optimised S_0 , S_1 , and T_1 structures.

Table S3. Energy decomposition of the fluorescent shift for PTCDI on the hBN surface and the hBN/PTCDI/hBN sandwich structure calculated at the (TD-) ω B97X-D3-gCP/def2-SVP level of theory. All values are given in eV.

| System | E_{gas}^a | E_{dist}^b | E_{pc}^c | E_{ads}^d | ΔE_{dist}^e | ΔE_{elec}^f | ΔE_{chem}^g | ΔE_{tot}^h |
|---------------|--------------------|---------------------|-------------------|--------------------|----------------------------|----------------------------|----------------------------|---------------------------|
| PTCDI/hBN | 2.526 | 2.517 | 2.517 | 2.406 | 0.009 | 0.000 | 0.111 | 0.120 |
| hBN/PTCDI/hBN | 2.526 | 2.517 | 2.518 | 2.321 | 0.009 | -0.001 | 0.197 | 0.205 |

^a E_{gas} is $S_0 \leftarrow S_1$ transition energy of PTCDI at S_1 gas phase structure

^b E_{dist} is $S_0 \leftarrow S_1$ transition energy of PTCDI at S_1 (hBN)/PTCDI/hBN structure with removed hBN

^c E_{pc} is $S_0 \leftarrow S_1$ transition energy of PTCDI at S_1 (hBN)/PTCDI/hBN structure with hBN atoms replaced by calculated point charges

^d E_{ads} is $S_0 \leftarrow S_1$ transition energy of PTCDI at S_1 (hBN)/PTCDI/hBN structure

^e $\Delta E_{\text{dist}} = E_{\text{gas}} - E_{\text{dist}}$ (contribution from molecular distortion)

^f $\Delta E_{\text{elec}} = E_{\text{dist}} - E_{\text{pc}}$ (contribution from electrostatic interactions)

^g $\Delta E_{\text{chem}} = E_{\text{pc}} - E_{\text{ads}}$ (contribution from chemical interactions)

^h $\Delta E_{\text{tot}} = \Delta E_{\text{dist}} + \Delta E_{\text{elec}} + \Delta E_{\text{chem}} = \Delta E_{\text{gas}} - \Delta E_{\text{ads}}$ (total fluorescent shift)

1.2 Resonant shifts

Further shifts in the fluorescence transition energy occur due to the coupling of the transition dipole moment of each molecule with the hBN encapsulating layers and with the dipole moments of neighbouring molecules¹². To obtain the intermolecular coupling we estimate the interaction between two point dipoles on neighbouring molecules and sum these pair interactions for the molecules present in a lattice as determined by the AFM images shown in the main text (Fig. 1b). For a PTCDI network adsorbed on hBN surface the effect of the intermolecular coupling on the fluorescence spectra has been considered in our previous work, and the corresponding red-shift of 0.059 eV was reported.¹⁰ In the case of a hBN/PTCDI/hBN sandwich structure a smaller shift is expected since: (i) the transition dipole moment is lower for the encapsulated molecule; (ii) the screening factor is increased from $(\epsilon + 1)/2$ to ϵ , where ϵ is the dielectric constant of hBN (we take the geometric average¹³ of $\epsilon = 3.5$). Using a simple scaling, the red shift for the encapsulated PTCDI is therefore expected to be 0.031 eV.

When considering the interactions of a PTCDI molecule with the hBN encapsulating layers, the transition dipole cannot be considered as point-like since for this planar molecule the charge fluctuations giving rise to the dipole moment are distributed over a length scale greater than the

molecule-substrate separation. In our previous work¹⁰ we used the extended dipole model¹⁴ to describe the charge distribution in PTCDI; in this one-dimensional model the dipole is represented as two point charges separated by a fixed distance, and the values of charge and separation are determined from the transition density derived from our density functional calculations. In subsequent studies on the adsorption of metal-free phthalocyanine¹⁵ we used a more general model to capture the dependence of the variation of the transition density in two dimensions; in this case the interaction of the full transition density with its image charge was calculated. Using the results of the density functional calculations we have determined the shift using both approaches and the results are tabulated below in Tables S4 and S5.

Table S4. Resonant shift induced in PTCDI due to the interaction of the transition dipole moment with hBN layers, relative to the molecule in the gas phase.

| Model | PTCDI adsorbed on hBN (eV) | PTCDI encapsulated in hBN (eV) | Difference |
|-----------------------|----------------------------|--------------------------------|------------|
| 2D transition density | 0.054 | 0.057 | 0.003 |
| Extended dipole | 0.094 | 0.122 | 0.028 |

Interestingly, when combined with the decrease from 0.059 eV to 0.031 eV associated with the reduction in coupling of neighbouring transition dipoles (see above), the total resonant red shift due to an addition of a second hBN layer has a small negative value of -0.025 eV for the transition density model, and is close to zero for the extended dipole model. This result is slightly counterintuitive but is a consequence of the reduction of transition dipole moment and changes to the transition density. The overall expected red shift when a second hBN layer is added is therefore dominated by the non-resonant shift as shown in Supplementary Table 5 and, depending on assumptions, is in the range 0.060 - 0.085 eV in very good agreement with the observed additional shift, 0.08 eV (see main paper). Combining these data with the results discussed above gives, for the transition density model, transitions energies of 2.26 eV and 2.20 eV for uncapped and capped PTCDI respectively; these values are quoted in the main paper.

Table S5. Summary of the calculated shifts (in eV) due to the non-resonant interactions with the substrate and for a range of resonant interactions, relative to the molecule in the gas phase.

| System | Non Resonant | | Resonant | | Total |
|---------------|-----------------|-----------------|---------------|-----------------------|---------------|
| | Substrate (DFT) | H-bonding (DFT) | Substrate | Screened TDM coupling | |
| PTCDI/hBN | 0.120 | 0.030 | 0.054 – 0.094 | 0.059 | 0.263 – 0.303 |
| hBN/PTCDI/hBN | 0.205 | 0.030 | 0.057 – 0.122 | 0.031 | 0.323 – 0.388 |

2. Experimental Methods

2.1 Molecular deposition

hBN was exfoliated onto SiO₂(90 nm)/Si wafers and then loaded into a vacuum chamber (base pressure 1×10^{-8} mbar). The samples were initially annealed to 450 °C and, subsequently, a 0.5 monolayer (ML) coverage of PTCDI was deposited at a rate of 0.3 ML/min at a substrate temperature, 150 °C; under these conditions, islands with monolayer height and lateral dimensions of 5.2 μ m were obtained.

2.2 Heterostructure assembly

Graphene and hBN were exfoliated onto SiO₂/Si wafers using the scotch tape method (M3 Scotch tape). The hBN wafers were then briefly flame annealed¹⁶. Few-layer graphene and hBN flakes, and individual islands of PTCDI were identified using optical microscopy (see Figure S4). To assemble the heterostructures we prepared polymer stamps, consisting of a glass slide coated with Sylgard® 184 polydimethylsiloxane and polypropylene carbonate (15 % by weight in anisole, Merck). To pick up flakes (or partially formed heterostructures) the stamp is brought into contact with a target flake/heterostructure which is heated to 45 °C. The stamp is then retracted and removes the selected flake from the substrate. To release a flake/heterostructure the stamp is brought into contact with the substrate initially at a temperature 45 °C after which the substrate is heated to 110 °C and the stamp is retracted leaving the flake/heterostructure on the surface. The structure is then cleaned by immersion in chloroform (Honeywell) to

remove residual polymer. Each pick-up and release cycle results in the addition of one layer to the heterostructure and the relative placement of the layer is monitored using optical microscopy. After the sequential addition of the upper contact and hBN barriers, the partially-formed heterostructure is deposited on a SiO₂/Si wafer on which; (i) metal leads (10 nm Cr/30 nm Au) had been pre-deposited using a shadow mask; (ii) the lower graphene contact and a thick hBN supporting flake had been transferred using the dry transfer technique.

During and after fabrication, AFM images were acquired using either an Asylum Research Cypher S or MFP-3D, in combination with NuNano Scout 70 cantilevers to keep track of flake thicknesses and to ensure the integrity of the active region of the device.

2.3 Electrical and optical measurements

Electrical measurements were carried out at room temperature or at liquid helium temperatures using a Keithley Sourcemeter (1612B) with the sample under vacuum ($\sim 10^{-6}$ mbar) in an Oxford Instruments Microstat He flow-cryostat. We used a Horiba MicOS optical spectrometer with a 50x objective, NA: 0.5, and 150 l/mm grating to acquire spectra through an optical window. Photoluminescence measurements were acquired using a 405 nm pulsed delta diode excitation source, with a pulse rate of 100 MHz with a time-averaged power ~ 10 μ W and a spot size of approximately 2 μ m.

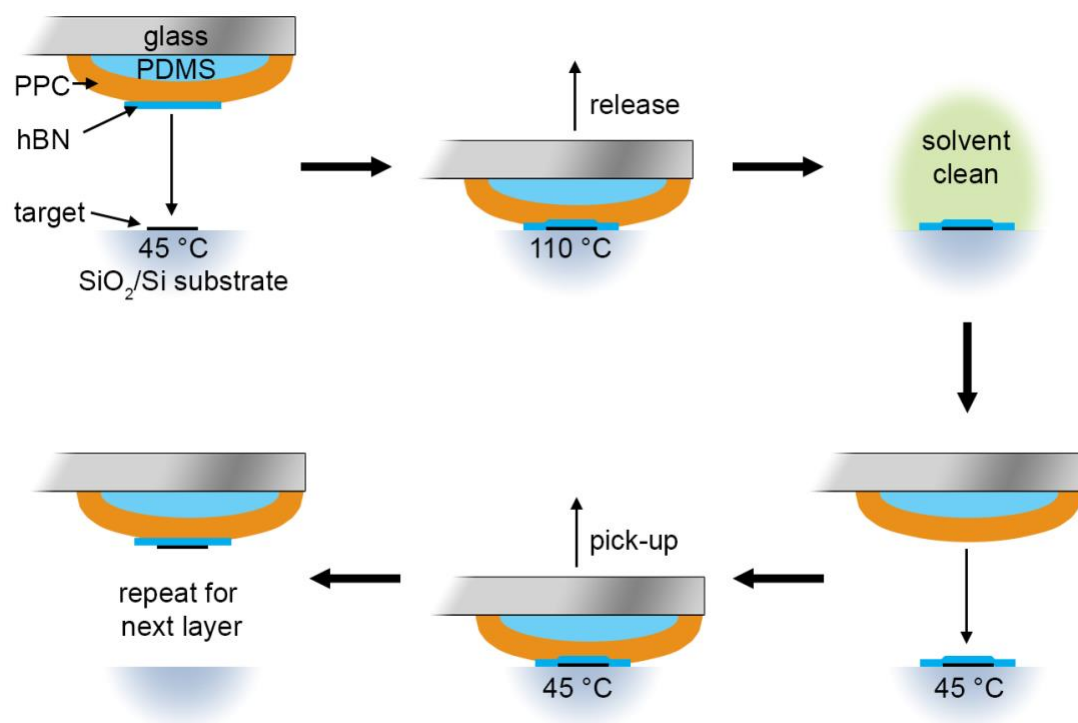


Figure S4. Schematic showing the technique for pick-up and release of flakes of 2D materials including those on which molecular monolayers are deposited.

3. Additional Data

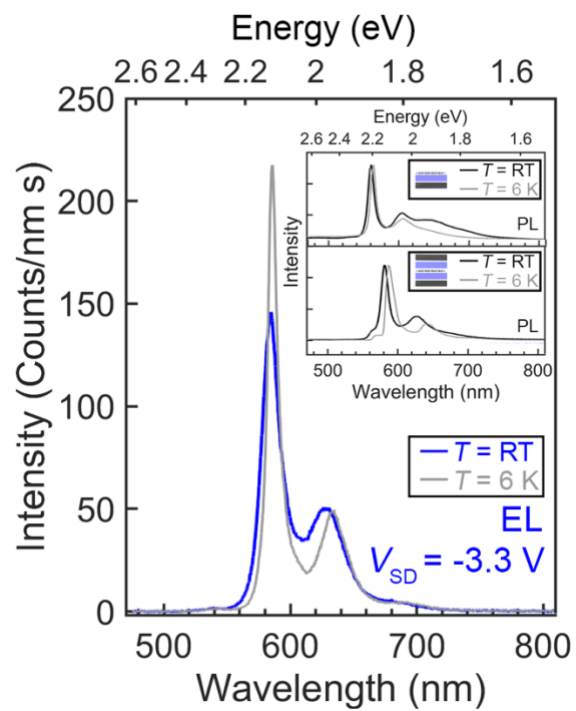


Figure S5. Comparison of electroluminescence and photoluminescence (inset: upper – uncapped, lower capped) spectra at room temperature and low temperature.

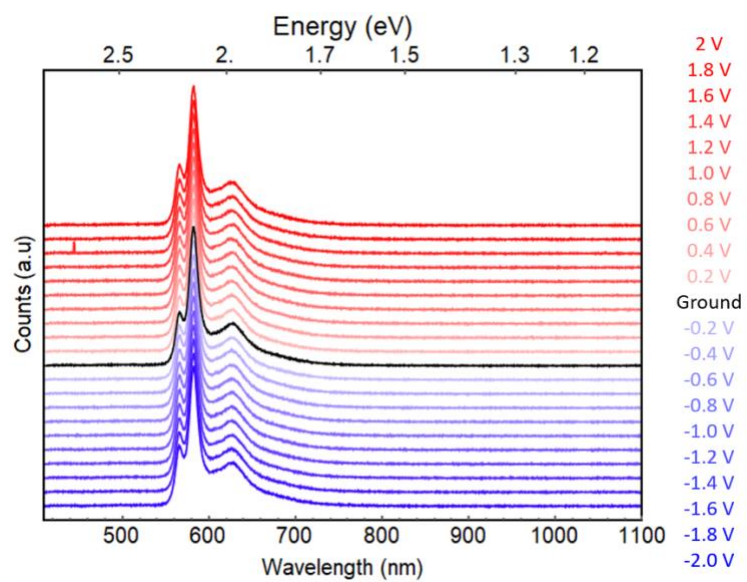


Figure S6. Photoluminescence spectra acquired from the active region of the device shown in Fig. 2. The data show that the spectra negligible variation of spectra over this voltage range.

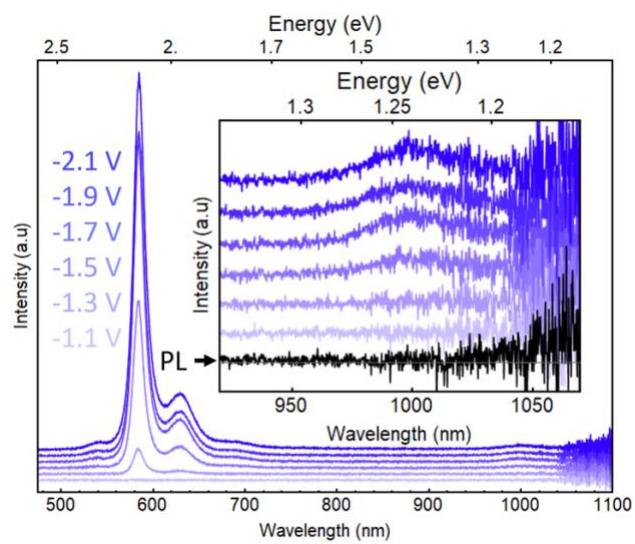


Figure S6. EL spectra acquired at room temperature at low applied voltage for device discussed in Figure 3. EL emission is observed for voltages as low as $|eV_{SD}| = 1.3\text{V}$.

References

1. Lin, Y. S., Li, G. De, Mao, S. P. & Chai, J. Da. Long-range corrected hybrid density functionals with improved dispersion corrections. *J. Chem. Theory Comput.* **9**, 263–272 (2013).
2. Weigend, F. & Ahlrichs, R. Balanced basis sets of split valence, triple zeta valence and quadruple zeta valence quality for H to Rn: Design and assessment of accuracy. *Phys. Chem. Chem. Phys.* **7**, 3297 (2005).
3. Weigend, F. Accurate Coulomb-fitting basis sets for H to Rn. *Phys. Chem. Chem. Phys.* **8**, 1057 (2006).
4. Grimme, S., Antony, J., Ehrlich, S. & Krieg, H. A consistent and accurate ab initio parametrization of density functional dispersion correction (DFT-D) for the 94 elements H-Pu. *J. Chem. Phys.* **132**, 154104 (2010).
5. Grimme, S., Ehrlich, S. & Goerigk, L. Effect of the damping function in dispersion corrected density functional theory. *J. Comput. Chem.* **32**, 1456–1465 (2011).
6. Kruse, H. & Grimme, S. A geometrical correction for the inter- and intra-molecular basis set superposition error in Hartree-Fock and density functional theory calculations for large systems. *J. Chem. Phys.* **136**, 154101 (2012).
7. Breneman, C. M. & Wiberg, K. B. Determining atom-centered monopoles from molecular electrostatic potentials. The need for high sampling density in formamide conformational analysis. *J. Comput. Chem.* **11**, 361–373 (1990).
8. Neese, F. Software update: the ORCA program system, version 4.0. *Wiley Interdiscip. Rev. Comput. Mol. Sci.* **8**, e1327 (2018).
9. Neese, F. Efficient and accurate approximations to the molecular spin-orbit coupling operator and their use in molecular g-tensor calculations. *J. Chem. Phys.* **122**, 034107

- (2005).
10. Kerfoot, J. *et al.* Substrate-induced shifts and screening in the fluorescence spectra of supramolecular adsorbed organic monolayers. *J. Chem. Phys.* **149**, 054701 (2018).
 11. Hochheim, M. & Bredow, T. Adsorption-induced changes of intramolecular optical transitions: PTCDA/NaCl and PTCDA/KCl. *J. Comput. Chem.* **36**, 1805–1811 (2015).
 12. Müller, M., Paulheim, A., Eisfeld, A. & Sokolowski, M. Finite size line broadening and superradiance of optical transitions in two dimensional long-range ordered molecular aggregates. *J. Chem. Phys.* **139**, 044302 (2013).
 13. Mele, E. J. Screening of a point charge by an anisotropic medium : Anamorphoses in the method of images Screening of a point charge by an anisotropic medium : Anamorphoses in the method of images. *Am. J. Phys.* **69**, 557 (2001).
 14. Marguet, S. *et al.* Influence of Disorder on Electronic Excited States : An Experimental and Numerical Study of Alkylthiotriphenylene Columnar Phases. *J. Phys. Chem. B* **102**, 4697–4710 (1998).
 15. Alkhamisi, M. *et al.* The growth and fluorescence of phthalocyanine monolayers, thin films and multilayers on hexagonal boron nitride. *Chem. Commun.* **1**, 12021–12024 (2018).
 16. Kerfoot, J. *et al.* Two-Dimensional Diffusion of Excitons in a Perylene Diimide Monolayer Quenched by a Fullerene Heterojunction. *J. Phys. Chem. C* **123**, 12249–12254 (2019).